Mon. Not. R. Astron. Soc. **380,** 963–978 (2007) doi:10.1111/j.1365-2966.2007.12183.x

Fundamental differences between SPH and grid methods

Oscar Agertz,[1⋆] Ben Moore,[1] Joachim Stadel,[1] Doug Potter,[1] Francesco Miniati,[2] Justin Read,[1] Lucio Mayer,[2] Artur Gawryszczak,[3] Andrey Kravtsov,[4] Åke Nordlund,[5] Frazer Pearce,[6] Vicent Quilis,[7] Douglas Rudd,[4] Volker Springel,[8] James Stone,[9] Elizabeth Tasker,[10] Romain Teyssier,[11] James Wadsley[12] and Rolf Walder[13]

[1]*Institute for Theoretical Physics, University of Zürich, CH-8057 Zürich, Switzerland*
[2]*Department of Physics, Institute für Astronomie, ETH Zürich, CH-8093 Zürich, Switzerland*
[3]*Nicolaus Copernicus Astronomical Centre, Bartycka 18, Warsaw PL-00-716, Poland*
[4]*Department of Astronomy & Astrophysics, The University of Chicago, Chicago, IL 60637, USA*
[5]*Niels Bohr Institute, Copenhagen University, Juliane Maries Vej 30, DK-2100 København Ø, Denmark*
[6]*School of Physics and Astronomy, University of Nottingham, University Park, Nottingham NG7 2RD*
[7]*Departemento de Astronomia y Astrofisica, Universidad de Valencia, 46100 Burjasott, Valencia, Spain*
[8]*Max-Planck-Institute for Astrophysics, Karl-Schwarzschild-Str. 1, 85740 Garching, Germany*
[9]*Department of Astrophysical Sciences, Princeton University, Princeton, NJ 08544, USA*
[10]*Department of Astronomy, Columbia University, New York, NY 10027, USA*
[11]*Service d'Astrophysique, CEA/DSM/DAPNIA/SAp, Centre d'Etudes de Saclay, L'orme des Merisiers, 91191 Gif-sur-Yvette Cedex, France*
[12]*Department of Physics and Astronomy, McMaster University, Hamilton, Ontario L88 4M1, Canada*
[13]*Institute für Astronomie, ETH Zürich, CH-8092 Zürich, Switzerland*

Accepted 2007 July 3. Received 2007 June 30; in original form 2006 October 16

ABSTRACT

We have carried out a comparison study of hydrodynamical codes by investigating their performance in modelling interacting multiphase fluids. The two commonly used techniques of grid and smoothed particle hydrodynamics (SPH) show striking differences in their ability to model processes that are fundamentally important across many areas of astrophysics. Whilst Eulerian grid based methods are able to resolve and treat important dynamical instabilities, such as Kelvin–Helmholtz or Rayleigh–Taylor, these processes are poorly or not at all resolved by existing SPH techniques. We show that the reason for this is that SPH, at least in its standard implementation, introduces spurious pressure forces on particles in regions where there are steep density gradients. This results in a boundary gap of the size of an SPH smoothing kernel radius over which interactions are severely damped.

Key words: hydrodynamics – instabilities – turbulence – methods: numerical – ISM: clouds – galaxies: evolution – galaxies: formation – galaxies: general.

1 INTRODUCTION

The ability to numerically model interacting fluids is essential to many areas of astrophysics and other disciplines. From the formation of a star and its protoplanetary disc to galaxies moving through the intracluster medium (ICM), dynamical instabilities such as Kelvin–Helmholtz (KH) and Rayleigh–Taylor (RT) play a fundamental role in astrophysical structure formation. Most popular hydrodynamical methods can be divided into two classes: techniques following the gas using Eulerian grids (e.g. Laney 1998; Leveque 1998) and those which follow the Lagrangian motions of gas particles such as 'smoothed particle hydrodynamics' (SPH; Monaghan 1992). Grid-based techniques solve the fluid dynamical equations by calculating the flux of information through adjacent cell boundaries, while SPH techniques calculate the gas properties on each particle by averaging over its nearest neighbours. Because of the extensive use, and sometimes discrepant results of these techniques, it is interesting to carry out code comparison studies on well-defined problems that test their ability to follow the basic gas physics they are designed to simulate. Recent code comparisons have been focusing on differences in a cosmological context (e.g. Frenk & et al 1999; O'Shea et al. 2005; Regan, Haehnelt & Viel 2007). They all find differences between grid and SPH codes but due to the complexity of these types of simulations it is not obvious how the differences arise. Similarly, while SPH studies of galaxy–ICM interactions by Abadi, Moore & Bower (1999) found that only half the interstellar medium was removed from the galaxy. Using a grid-based calculation with the same initial conditions (ICs), Quilis, Moore & Bower (2000) found that all the gas could be removed and attributed the difference to

⋆E-mail: agertz@physik.unizh.ch

the high resolution shock capturing ability of their Eulerian code. However, we are not aware of a direct comparison between simulation methods in this context. Differences were found in the literature between different studies of the same problem.

Our test problem is to follow cold dense gas cloud moving through a low-density hot medium. This is specifically designed to capture the same physical processes that occur during the formation and evolution of astrophysical structures. We will also study the shearing motion of two fluids of different densities to elucidate the problems that we find with this test. Similar configurations, including shock wave interaction with clouds, have been studied by e.g. Murray et al. (1993), Klein, McKee & Colella (1994), Mac Low & Zahnle (1994), Mac Low et al. (1994), Vietri, Ferrara & Miniati (1997) and Mori & Burkert (2000).

The paper is organized as follows. In Section 2 we briefly describe the main features of the test problem followed by analytical expectations in Section 3. In Section 4 we describe our numerical implementation of the set-up as well as all codes used in our comparison. In Section 5 we present the results of our simulations followed by an explanation of the found discrepancies in Section 6. In Section 7 we summarize our results and briefly discuss their implications.

2 THE BLOB TEST

A schematic view of the blob test problem can be seen in Fig. 1. A spherical cloud of gas is placed in a wind tunnel with periodic boundary conditions. The ambient medium is 10 times hotter and 10 times less dense than the cloud so that it is in pressure equilibrium with the latter. We will refer to this initial density contrast between the cloud and the medium as $\chi_{\rm ini}$. All of the gas is atomic hydrogen with molecular weight $\mu = 1.0$ and an adiabatic index $\gamma = 5/3$.

This set-up is useful to investigate how different simulation codes handle typical astrophysical processes important for multiphase systems, such as ram-pressure stripping and fragmentation through KH instabilities (KHIs) and RT instabilities (RTIs).

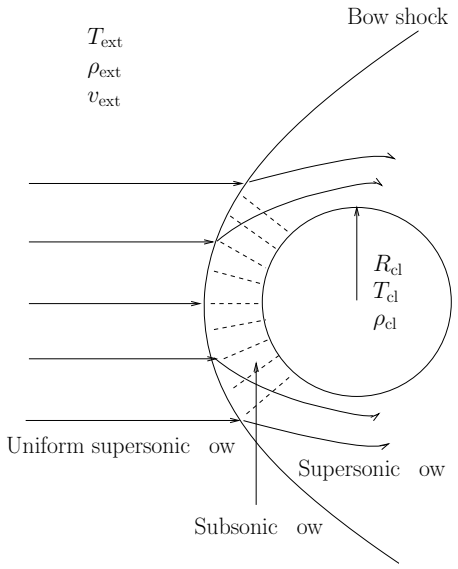

Figure 1. Illustration of the blob test. The external medium, which initially is in pressure equilibrium with the cloud, travels with a supersonic velocity creating a bow shock in front of the cloud. The post-shock flow is subsonic until the smooth flow accelerates and again obtains supersonic speed on the lateral sides of the cloud.

3 ANALYTICAL EXPECTATIONS

Although the non-linear stages of the KHIs and RTIs cannot be fully described analytically, we can still use analytic arguments to estimate the characteristic disruption time-scale for the cloud.

In order to specify our problem we characterize the external medium with a sound speed $c_{\rm s}$ and assign it an initial velocity $v_{\rm ext} = \mathcal{M} c_{\rm s}$ with Mach number $\mathcal{M} = 2.7$. Furthermore, we place the cloud initially at rest in the computational domain. Since the wind is supersonic, a bow shock will form in front of the cloud with the post-shock properties given by the Rankine–Hugoniot shock jump conditions. Because the cloud is accelerated by the wind, we will from now on perform all of our calculations in the rest frame of the bow shock, referring to pre-shock quantities with the subscript 1 and post-shock with 2. The shock conditions for the density, velocity and Mach number are (e.g. Shu 1992)

$$\frac{\rho_2}{\rho_1} = \frac{v_1}{v_2} = \frac{(\gamma+1)\mathcal{M}_1^2}{(\gamma+1)+(\gamma-1)\left(\mathcal{M}_1^2-1\right)}, \tag{1}$$

$$\mathcal{M}_2^2 = \frac{2+(\gamma-1)\mathcal{M}_1^2}{2\gamma\mathcal{M}_1^2-(\gamma-1)}. \tag{2}$$

Formally we would take the obliqueness of the bow shock into account but for simplicity we will only consider the flow that enters at the symmetry axis of the cloud.

The cloud acceleration can be approximated by considering the maximum area that can gain momentum from the ambient flow. This implies that all gas in a cylinder in front of the cloud transfers momentum leading to an acceleration

$$a_{\rm cl} \sim \dot{v}_1 \sim \frac{\rho_{\rm ext}\pi R_{\rm cl}^2 v_1^2}{M_{\rm cl}}. \tag{3}$$

Integrating this equation leads us to the evolution of the pre-shock velocity

$$v_1(t) = \frac{l}{(t + l/v_{\rm ext})}, \tag{4}$$

where l is a characteristic length given by $l = M_{\rm cl}/2\pi R_{\rm cl}^2\rho_{\rm ext}$. By using equation (4) to calculate the pre-shock Mach number together with equation (2) we can obtain a qualitative understanding of the post-shock velocity. This velocity is crucial for the stability of the cloud surface and, as we will show in Section 3.1, for the destruction of the cloud itself. The evolution of the post-shock Mach number $\mathcal{M}_2$ is given by

$$\mathcal{M}_2^2 = \begin{cases} \frac{2+(\gamma-1)(v_1/c_{\rm s})^2}{2\gamma(v_1/c_{\rm s})^2-(\gamma-1)} & \text{for } t < t_{\rm sonic}, \\ (v_1/c_{\rm s})^2 & \text{for } t > t_{\rm sonic}. \end{cases} \tag{5}$$

Here $t_{\rm sonic}$ is the time at which $\mathcal{M}_1 = \mathcal{M}_2 = 1$ and the shock disappears. After this point, gas freely streams towards the cloud and the Mach number decreases only due to the continued acceleration. Notice that for $t < t_{\rm sonic}$, $\mathcal{M}_2 < 1$, even for $\mathcal{M}_1 = v_1/c_{\rm s} \to \infty$. This means that behind the shock, the flow will always be subsonic and we expect instabilities to grow there. For $t \to \infty$, $\mathcal{M}_2 \to 0$ and the cloud will eventually be comoving with the background flow. The evolution of the post-shock Mach number is shown in Fig. 2 in terms of the so-called 'crushing time' defined as, in our notation,

$$\tau_{\rm cr} = \frac{2R_{\rm cl}\chi^{1/2}}{v_1}, \tag{6}$$

where χ is the density contrast between the cloud and the external medium. This is a natural time-scale supersonic cloud evolution. We will naively use $\chi = \chi_{\rm ini} = 10$ and $v_1 = v_{\rm ext}$, representing our IC.

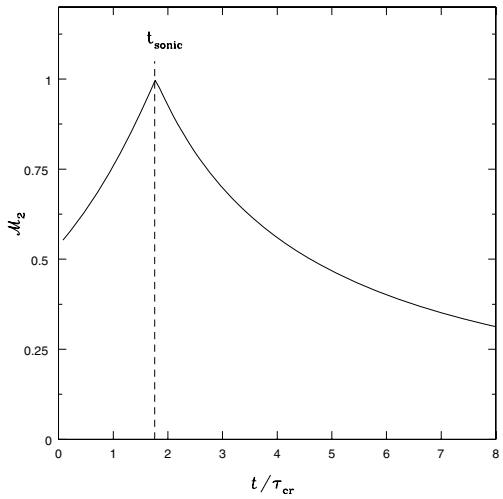

Figure 2. We plot the Mach number of the flow directly downstream of the shock on the symmetry axis of the cloud. The flow speed increases due to the weakened shock strength up to $t_{\rm sonic}$ where the relative motion of the cloud and wind turns subsonic.

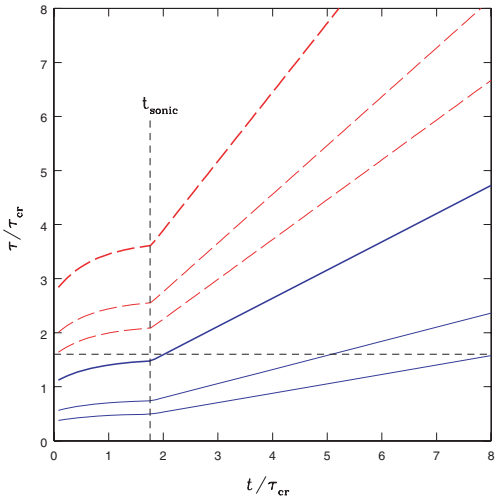

Figure 3. The time dependence of the growth rates of KHIs (solid, blue lines) and RTIs (dashed, red lines). The lines represent different sizes of perturbation wavelengths: $R_{\rm cl}$ (thick), $R_{\rm cl}/2$ (middle) and $R_{\rm cl}/3$ (thin).

During the interval of $\tau_{\rm cr}$ a bow shock is formed and the shocked gas will form a smooth flow around the cloud, reaching supersonic speed at the points indicated in Fig. 1. Beyond this region we expect to see a turbulent boundary layer forming which transports material off the surface. The cloud will compress along the line of motion due to an internal shock wave generated by the external gas. From Bernoulli's theorem we know that the pressure is low on the lateral sides which causes an overspilling of the cloud due to the high inner pressure of the compressed cloud (Doroshkevich & Zeldovich 1981). This causes mass loss irrespective of any instability.

3.1 The Kelvin–Helmholtz instability

KHIs occur when velocity shear is present at the interface between two fluids. The importance of the KHIs, in the context of gas cloud stability, has been studied by many authors e.g. Nulsen (1982), Murray et al. (1993), Vietri et al. (1997) and Mori & Burkert (2000).

Neglecting gravity, the dispersion relation of the KHIs, in the notation of our set-up, for an incompressible fluid is (Chandrasekhar 1961)

$$w = k\frac{(\rho_2\rho_{\rm cl})^{1/2}v_2}{(\rho_2+\rho_{\rm cl})} \approx \frac{kv_2}{\chi^{1/2}}, \tag{7}$$

where k is the wavenumber of the instability and the last approximation holds for $\chi \gg 1$. The characteristic growth time for the KHIs is then

$$\tau_{\rm KH} \equiv \frac{2\pi}{w} = \frac{2\pi(\rho_2+\rho_{\rm cl})}{k(\rho_2\rho_{\rm cl})^{1/2}v_2} \approx \frac{2\pi\chi^{1/2}}{kv_2}. \tag{8}$$

By naively using the post-shock quantities of equation (1) and our choice of cloud parameters, we can calculate an approximate time dependence of the KHIs, which is shown in Fig. 3 (blue, solid lines), for perturbations of size $R_{\rm cl}$ (thick), $R_{\rm cl}/2$ (middle) and $R_{\rm cl}/3$ (thin). Small-scale instabilities grow faster due to the $\tau_{\rm KH} \sim k^{-1}$ relation. The first modes to grow are the shortest. Their growth will act to widen the interface between the shearing layers, hence dampening the growth of modes smaller than the thickness of the interface (Chandrasekhar 1961). The fastest growing modes are now those that are equal to the thickness of the interface. As this process continues, the mode responsible for the cloud destruction is that which is comparable to the size of the cloud itself: $k_{\rm cl} \sim 2\pi/R_{\rm cl}$ (Nulsen 1982; Murray et al. 1993).

The instability growth time is always larger than the cloud crushing time. The horizontal line at $\tau = 1.6\tau_{\rm cr}$ in Fig. 3 indicates roughly the time at which the $k_{\rm cl}$ KH mode should have grown fully. We will from now on refer to this time as $\tau_{\rm KH}$.

Note that cloud compressibility can be taken into account when calculating the KH growth time (see Vikhlinin, Markevitch & Murray 2001), but was omitted for simplicity. Also note that in certain more physically motivated situations with external gravitational fields, self-gravity, physical viscosity, magnetic fields, radiation etc., the KHI is modified and is damped in most but not all cases (e.g. Murray et al. 1993; Vietri et al. 1997; Miniati, Jones & Ryu 1999; Gregori et al. 2000).

3.2 The Rayleigh–Taylor instability

RTIs occur when a denser fluid is accelerated by a less dense fluid. The cloud is accelerated with respect to the background and we expect RTIs to develop. The dispersion relation for the RTIs is (Chandrasekhar 1961)

$$|w^2| = k'a\left(\frac{\rho_{\rm cl}-\rho_{\rm ext}}{\rho_{\rm cl}+\rho_{\rm ext}}\right) \approx k'a, \tag{9}$$

where the last approximation is valid for $\chi \gg 1$. The KHI, which results from shearing flows, has a two-dimensional (2D) geometry, and can be described by as single wavevector k. By contrast, the RTI necessarily has a three-dimensional (3D) geometry and must be described by a vector wavelength, $\underline{k}' = (k_1, k_2)$, of magnitude $k' = \sqrt{k_1^2 + k_2^2}$. The acceleration on the surface can be assumed to be $a = \epsilon\, a_{\rm cl}$, where $a_{\rm cl}$ is given by equation (3) and ϵ is an efficiency factor. Note that it is very difficult to analytically determine the efficiency of the momentum transfer from the external medium on to the cloud. By using $\epsilon = 1$ we will get a lower limit on $\tau_{\rm RT}$.

Fig. 3 shows, for our choice of parameters, the characteristic growth times for RTIs (red, dashed lines) of size $R_{\rm cl}$ (thick), $R_{\rm cl}/2$ (middle) and $R_{\rm cl}/3$ (thin), demonstrating that $\tau_{\rm KH} < \tau_{\rm RT}$ for large instabilities. The largest mode grows very slowly and is probably not important in this type of problem. However, we expect that a fast

growing small-scale RTI should develop on the cloud front, especially on the axis of symmetry as the flow rams into the stagnation point. Complicated mixtures of KHIs and RTIs during later evolution are also expected until the cloud becomes fully comoving with the flow.

4 NUMERICAL SIMULATIONS

Our numerical simulations solve the Euler equations which neglect physical viscosity and radiative processes; we assume a perfect gas equation of state $P = R\rho T/M$, where R is the gas constant and M is the molar mass. Away from shocks, the evolution is strictly adiabatic. This means the gas can only undergo reversible heating and cooling by adiabatic compression or expansion, or irreversible heating in shocks. In order to isolate the differences in hydrodynamic solvers, we neglect the self-gravity of the gas.

4.1 Initial conditions

The ICs for the blob test are set up in the following way: we use a periodic simulation box of size, in units of the cloud radius $R_{\rm cl}$ $\{L_x, L_y, L_z\} = \{10, 10, 40\}$ and we centre the cloud at $\{x, y, z\} = \{5, 5, 5\}$. The ICs are generated by randomly placing equal mass particles to obtain the correct densities and cloud radius. Using an SPH code, the system is evolved and allowed to relax to obtain pressure equilibrium. By repeatedly adding small random velocities to the particles and letting the system relax we obtain a glass-like IC. Random velocities from spurious pressure forces will in this way be minimized compared to a completely random IC. Once the glass is created, the streaming velocity $v_{\rm ext}$ is given to the particles constituting the hot ambient medium. Because of the glass IC we note that the random velocities coming from spurious pressure forces are $\lesssim$ few per cent of $v_{\rm ext}$. One could smoothly increase the velocities to be more faithful to astrophysical situations, but this more violent start together with particle noise serves as the initial seed for surface instabilities of the cloud. Formally this can be seen as a triggering of small-scale RTI and Richtmyer–Meshkov instability. The Richtmyer–Meshkov instability occurs when a contact discontinuity gets shocked or rapidly accelerated. This generates vorticity and structures similar to those of RT (e.g. Inogamov 1999).

This particle set-up is used as IC for the SPH simulations. The ICs for the grid simulations are obtained by smoothing the gas quantities (density, temperature and velocities) on to each cell centre using the same spline kernel as in the SPH codes (see Section 4.2) using 32 nearest neighbours. In this way we have a consistent set-up for both of the methods and the noise introduced by using discrete particles in the SPH simulations is also present in the grid IC. As we will argue below, the key parameters to study are those connected with the resolution and strength of artificial viscosity (AV) therefore our parameter space studies will focus on the effect of these.

4.2 The codes

The simulation was carried out with about a dozen different independent simulation codes. Since all the grid codes gave consistent results, and similar for the SPH codes, we shall just present the detailed analysis of a selection of these codes which are summarized in Table 1. Here we give a brief description of these codes and the methods used for solving the hydrodynamical equations.

Table 1. Simulation details. ENZO and ART use the static grids indicated in the table while the CHARM and FLASH simulations have been run using AMR up to the indicated resolution. All static grid as well as the FLASH simulations were initialized using the stated resolution, CHARM started from 32, 32, 128.

nParticles/grid size	AV	Name
ART, static		
64, 64, 256	No AV	ART_64
128, 128, 512	No AV	ART_128
256, 256, 1024	No AV	ART_256
CHARM, AMR		
512, 512, 2048	No AV	CHARM_512
ENZO-PPM, static		
64, 64, 256	No AV	ENZO_64
128, 128, 512	No AV	ENZO_128
256, 256, 1024	No AV	ENZO_256
ENZO-ZEUS, static		
256, 256, 1024	$Q_{\rm AV} = 2.0$	ENZO_ZEUS1
256, 256, 1024	$Q_{\rm AV} = 0.5$	ENZO_ZEUS2
256, 256, 1024	$Q_{\rm AV} = 0.1$	ENZO_ZEUS3
FLASH, AMR		
64, 64, 256	No AV	FLASH_64
128, 128, 512	No AV	FLASH_128
256, 256, 1024	No AV	FLASH_256
GADGET-2		
10^7	$\alpha = 0.8$	GAD_10M
GASOLINE		
10^6	$\alpha = 1.0, \beta = 2.0$	GAS_1M
10^7	$\alpha = 1.0, \beta = 2.0$	GAS_10M
10^7	$\alpha = 0, \beta = 2.0$	GAS_10MAV1
10^7	$\alpha = 0, \beta = 0.5$	GAS_10MAV2
10^7	$\alpha = 0, \beta = 0.1$	GAS_10MAV3
10^7	Balsara, $\alpha = 1.0, \beta = 2.0$	GAS_BALS

4.2.1 ART (AMR)

ART (Adaptive Refinement Tree) is a N-body+gas dynamics AMR (Adaptive Mesh Refinement) code (Kravtsov 1999; Kravtsov, Klypin & Hoffman 2002). The ART code uses second-order shock-capturing Godunov-type solver (Colella & Glaz 1985) to compute numerical fluxes of gas variables through each cell interface, with 'left' and 'right' states estimated using piecewise linear reconstruction (van Leer 1979). This is a monotone method that is known to provide good results for a variety of flow regimes and resolves shocks within $\approx$1$-$2 cells. A small amount of dissipation in the form of artificial diffusion is added to numerical fluxes (Colella & Woodward 1984), as is customary in the shock-capturing codes. The details of the flux evaluation and summation on mesh interfaces can be found in Khokhlov (1998). In the simulations presented in this paper, a new distributed MPI version of the ART code developed by Douglas Rudd and Andrey Kravtsov was used (Rudd & Kravtsov, in preparation).

4.2.2 CHARM (AMR)

CHARM is an N-body+gas dynamics, AMR code, based on the CHOMBO-AMR library, employing a higher order Godunov's

method for the solution of the hydrodynamic equations (Miniati & Colella 2006). Here a piecewise linear reconstruction scheme with Van Leer's limiter and a non-linear Riemann solver were used, resulting in a second-order accurate method in both space and time. CHARM was used to test the influence of ICs on the cloud evolution.

4.2.3 ENZO-PPM (AMR)

ENZO[1] is an Eulerian AMR hybrid code (*N*-body+gas dynamics) that was originally written by Greg Bryan and Michael Norman at the National Center for Supercomputing Applications at the University of Illinois (Bryan & Norman 1997). ENZO uses the piecewise parabolic method (Colella & Woodward 1984, PPM) for solving fluid equations and has been adapted for cosmology (Bryan et al. 1995). PPM is a higher order accurate version of Godunov's method with an accurate piecewise parabolic interpolation and a non-linear Riemann solver for shock conditions. The method is third order accurate in space and second order in time for fixed time-stepping. For variable time-stepping it is formally second order in space. This together with the Riemann solver results in a very accurate shock treatment compared to the SPH codes where AV is used. In all of our tests we used the dual energy formalism in ENZO. Formally, the use of this is only necessary in hyper-Machian flows ($E_{\rm therm}/E_{\rm tot} \sim 10^{-3}$) to keep the PPM solver stable, and hence makes little difference for our case.

4.2.4 ENZO-ZEUS (AMR)

ENZO includes an implementation of the finite-difference hydrodynamic algorithm employed in the compressible magnetohydrodynamics code ZEUS (Stone & Norman 1992a,b). Fluid transport is solved on a Cartesian grid using the upwind, monotonic advection scheme of van Leer (1977) within a multistep (operator split) solution procedure which is fully explicit in time. This method is formally second order accurate in space but first order accurate in time.

The ZEUS method uses a von Neumann–Richtmyer AV to smooth shock discontinuities that may appear in fluid flows and can cause a breakdown of finite-difference equations. The AV term is added in the source terms as

$$\rho\frac{\partial \boldsymbol{v}}{\partial t} = -\nabla p - \rho\nabla\phi - \nabla\cdot\boldsymbol{Q}, \tag{10}$$

$$\frac{\partial e}{\partial t} = -p\nabla\cdot\boldsymbol{v} - \boldsymbol{Q} : \nabla\boldsymbol{v}, \tag{11}$$

where $\boldsymbol{v}$ is the baryon velocity, ρ is the mass density, p is pressure, e is internal energy density of gas and $\boldsymbol{Q}$ is the AV stress tensor, such that

$$Q_{ii} = \begin{cases} Q_{\rm AV}\rho(\Delta v_i)^2 & \text{for } \Delta v_i < 0. \\ 0 & \text{otherwise} \end{cases} \tag{12}$$

and

$$Q_{ij} = 0 \quad \text{for } i \neq j. \tag{13}$$

Δx_i and Δv_i refer to the width of the grid cell along the ith axis and the corresponding difference in gas velocities across the grid cell, respectively. $Q_{\rm AV}$ is a constant that roughly tells us over how many grid zones we smooth shocks. While the correct Rankine–Hugoniot jump conditions are achieved, shocks are thus not treated as true discontinuities. This may cause unphysical pre-heating of gas upstream of the shock wave, as discussed in e.g. Anninos & Norman (1994) and O'Shea et al. (2005).

4.2.5 FLASH (AMR)

FLASH[2] is an AMR hybrid code (*N*-body+gas dynamics) developed by the ASC Center at the University of Chicago (Fryxell et al. 2000). The PPM hydrodynamical solver is formally accurate to second order in both space and time but performs the most critical steps to third- or fourth-order accuracy. For the simulations performed in this paper we have used the publicly available FLASH version 2.3 using AMR with maximum refinement up to the resolutions indicated in Table 1.

4.2.6 GASOLINE (*SPH*)

GASOLINE is a parallel Tree + SPH code, described in Wadsley, Stadel & Quinn (2004). The code is an extension to the *N*-body gravity code PKDGRAV developed by Stadel (2001). GASOLINE uses AV to resolve shocks and has an implementation of the shear reduced version (Balsara 1995) of the standard (Monaghan 1992) AV. GASOLINE solves the energy equation using the asymmetric form and conserves entropy closely. It uses a standard spline smoothing kernel (Monaghan 1992) with compact support for the softening of the gravitational and SPH quantities. The kernel is symmetrized by using kernel averaging (Hernquist & Katz 1989) and we smooth over the 32 nearest neighbours when estimating fluid quantities.

The AV is implemented by solving a momentum equation of the form

$$\frac{{\rm d}\boldsymbol{v}_i}{{\rm d}t} = -\sum_{j=1}^{n} m_j \left(\frac{P_i}{\rho_i^2} + \frac{P_j}{\rho_j^2} + \Pi_{ij}\right)\nabla_i W_{ij}, \tag{14}$$

where P_j is pressure, $\boldsymbol{v}_i$ is velocity, W_{ij} is the smoothing kernel and the AV term Π_{ij} is given by

$$\Pi_{ij} = \begin{cases} \frac{-\alpha(1/2)(c_i+c_j)\mu_{ij}+\beta\mu_{ij}^2}{(1/2)(\rho_i+\rho j)} & \text{for } \boldsymbol{v}_{ij}\cdot\boldsymbol{r}_{ij} < 0, \\ 0 & \text{otherwise,} \end{cases} \tag{15}$$

where

$$\mu_{ij} = \frac{h(\boldsymbol{v}_{ij}\cdot\boldsymbol{r}_{ij})}{\boldsymbol{r}_{ij}^2 + 0.01(h_i+h_j)^2}, \tag{16}$$

where $\boldsymbol{r}_{ij} = \boldsymbol{r}_i - \boldsymbol{r}_j$, $\boldsymbol{v}_{ij} = \boldsymbol{v}_i - \boldsymbol{v}_j$ and c_j is the sound speed. α and β are the coefficients used for setting the viscosity strength, and are essential for capturing shocks and preventing particle interpenetration. Note that the viscosity term vanishes for non-approaching particles and the β parameter is the SPH implementation of the Neumann–Richtmeyer AV. The commonly used values in the literature is $\alpha = 1$ and $\beta = 2$ which originally was proposed by Lattanzio et al. (1986) using Sod shock tube tests. Later we will carry out experiments with different values of α and β.

4.2.7 GADGET-2 (*SPH*)

The TreeSPH code GADGET-2[3] (Springel, Yoshida & White 2001; Springel 2005) is the updated version of the GADGET-1. The code is similar in character to GASOLINE but uses an entropy conserving formulation of SPH. This means that the thermodynamic state of

[1] ENZO is available at http://lca.ucsd.edu/portal/software/enzo

[2] FLASH is available at http://flash.uchicago.edu/website/home/

[3] GADGET-2 is available at http://www.mpa-garching.mpg.de/gadget/

each fluid element in GADGET-2 is defined through the specific entropy and not the specific thermal energy. GADGET-2 uses a somewhat different formulation of AV than GASOLINE. The viscosity term in equation (14) is here formulated as

$$\Pi_{ij} = -\frac{\alpha}{2}\frac{v_{ij}^{\rm sig} w_{ij}}{\rho_{ij}}, \tag{17}$$

where $v_{ij}^{\rm sig} = c_i + c_j - 3\, w_{ij}$ is the so-called signal velocity. Here $w_{ij} = \boldsymbol{v}_{ij} \cdot \boldsymbol{r}_{ij}/|\boldsymbol{r}_{ij}|$ is the relative velocity projected on to the separation vector provided particles approach each other. Like GASOLINE, GADGET uses a spline smoothing kernel (Monaghan 1992) and we employ smoothing over the 32 nearest neighbours. In our test we used the publicly available GADGET-2 version 2.01.

5 RESULTS OF THE SIMULATIONS

Fig. 4 shows central density slices of GASOLINE (GAS_10M), GADGET-2 (GAD_10M), ENZO (ENZO_256), FLASH (FLASH_256) and ART (ART_256). These are the high-resolution simulations with the default standard settings.

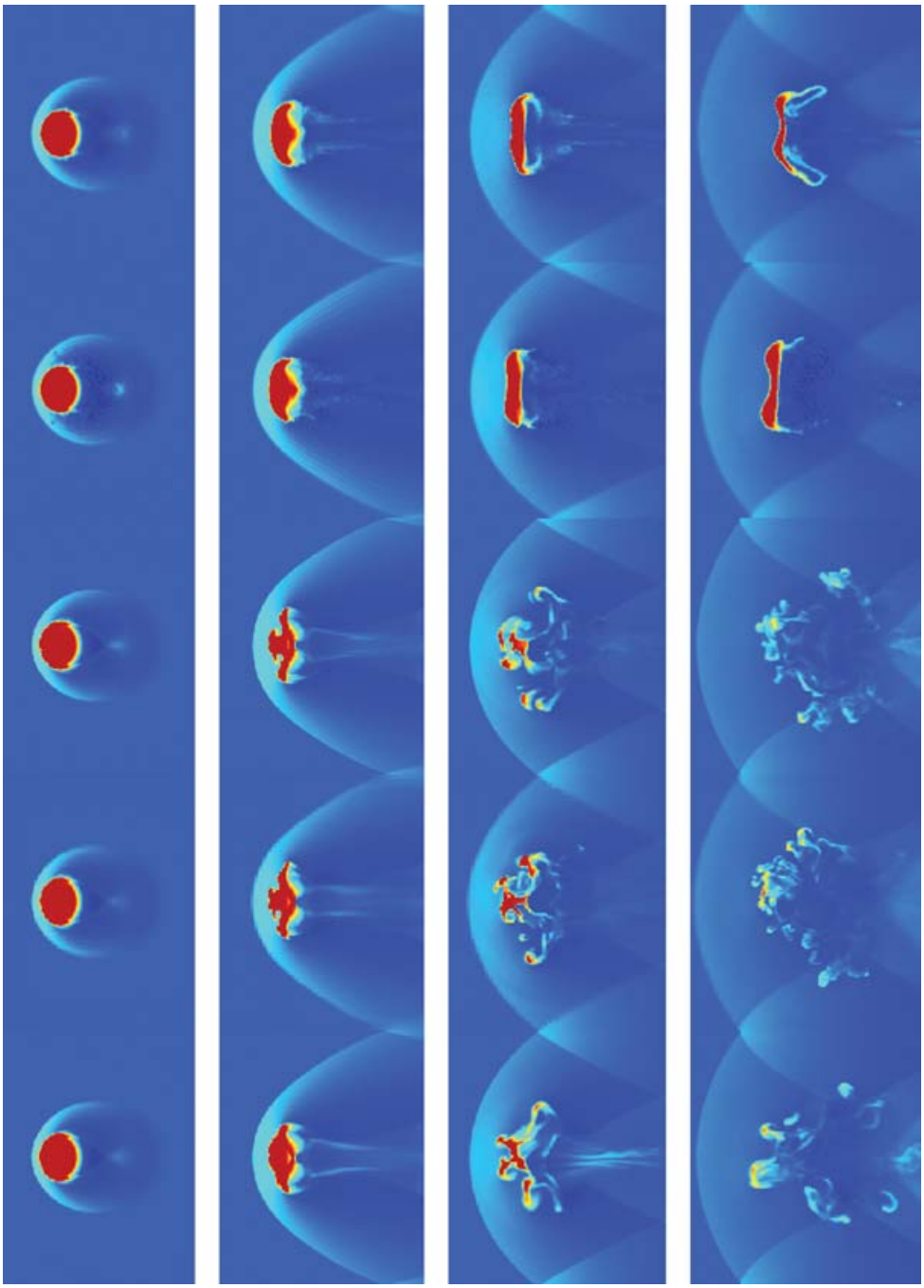

Figure 4. Gas density slices through the centre of the cloud at $t = 0.25$, 1.0, 1.75 and 2.5 $\tau_{\rm KH}$. From top to bottom we show GASOLINE (GAS_10M), GADGET-2 (GAD_10M), ENZO (ENZO_256), FLASH (FLASH_256) and ART-HYDRO (ART_256). The grid simulations clearly show dynamical instabilities and complete fragmentation after 2.5 $\tau_{\rm KH}$, unlike the SPH simulations in which most of the gas remains in a single cold dense blob.

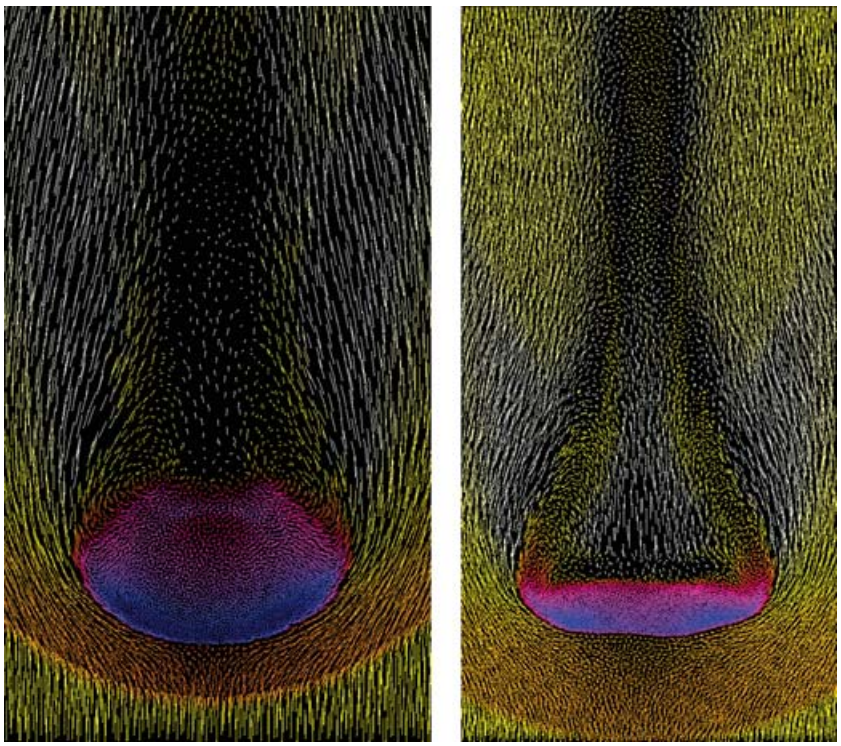

Figure 5. A thin central slice of the SPH particles of GAS_10M at $t = 0.75\,\tau_{\rm KH}$ (left-hand panel) and $t = 1.5\tau_{\rm KH}$ (right-hand panel). The density ranges from high (blue) to low (white) and the magnitude of the velocity vectors are normalized to the reference frame of the centre of the cloud. We clearly see the effect of the cloud stretching due to the lateral Bernoulli zones and the formation of downstream vorticity.

The simulations of the two SPH codes, GAS_10M and GAD_10M, show a very similar evolution. As expected, a detached bow shock forms directly in front of the cloud. An internal shock wave forms within the cloud compressing it. The post-shock flow encompasses the cloud, creating Bernoulli zones on the top and bottom with lower pressure. This causes the cloud to become elongated as well as compressed along the z-axis and we see gas being ablated, i.e. stripped through the induced pressure differences, from the top and bottom edges. Gas stripping slowly progresses and the cloud's shape does not change significantly for a long time. Fig. 5 shows the particles in a thin slice centred on the cloud. The velocity vectors of each particle are plotted in a reference frame centred on the cloud. The colours indicate the gas density. Behind the edges of the cloud we see a vortex created due to the shearing motion of the ambient medium which creates a low-pressure region behind the cloud.

Initially, the cloud evolution is similar in the grid simulations. It is compressed and elongated and gas is removed from the trailing edges where the vortex has created a vacuum behind the cloud. Some of the ambient medium is entrained in the turbulent wake behind the cloud and falls on to the backside of the cloud. However, the late cloud evolution is very different in these simulations. Early on we observe surface perturbations on the front of the cloud, probably originating from the way the ICs are set-up (see argument in Section 4.1). A complicated mixture of KHIs and RTIs are developing on the cloud front which, due to subsequent compression and lateral expansion, becomes even more KH and RT unstable. By $t \sim \tau_{\rm KH}$, large-scale KHIs have developed and the cloud starts to fragment. Further instabilities and turbulence mixes the smaller clumps of gas into the ambient medium. All grid simulations show basically the same cloud destruction time. We also note that Eulerian (shock capturing) methods effectively localize shocks to a few grid

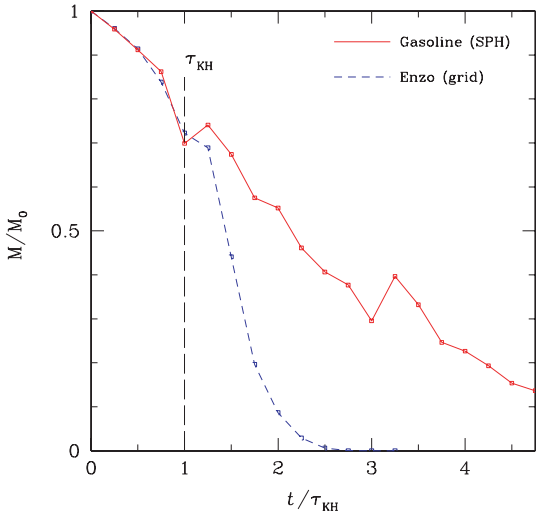

Figure 6. The evolution of the cloud mass fraction. In the SPH simulation (solid, red), the cloud slowly loses mass to the ambient medium and has not been completely mixed even after $5\tau_{\rm KH}$. The grid simulation (dashed, blue) follows the SPH up to the time at which the KHI causes it to rapidly fragment and mix.

cells compared to the smoothed out shocks in the SPH simulations resulting from AV shock capturing schemes. In Fig. 6 we show the remaining cloud mass fractions as a function of time for the ENZO and GASOLINE simulations. These are representative of grid and SPH methods. We define the cloud as being any gas that satisfies $T < 0.9\,T_{\rm ext}$ and $\rho > 0.64\rho_{\rm cl}$. It is of course possible to construct more

elaborate criteria but these select the gas that visually is a part of the cloud. The figure shows that both techniques give a similar mass loss up to $\sim \tau_{\rm KH}$. Before this time the gas loss is mainly due to ablation into the low-pressure zone created behind the cloud. As soon as we pass $\tau_{\rm KH}$ for large-scale KHIs the SPH and grid methods diverge. In the grid simulation, the cloud quickly disrupts and diffuses into the ambient medium, while the SPH simulation only shows continuing stripping. After $t = 2.5\tau_{\rm KH}$, no gas in the grid simulation can satisfy our criteria while the SPH simulation still shows a mass fraction $\approx$40 per cent. This shows us that the vortex shedding through the Bernoulli zones is the most important mechanism for mass loss at $t < \tau_{\rm KH}$ in both methods. After this time dynamical instabilities dominate the grid mass loss.

5.1 Resolution dependence

It is difficult to do a direct translation between grid and SPH resolution. The maximum allowed resolution is a fixed grid of size $256 \times 256 \times 1024$ in the grid runs and 10^7 particles in the SPH runs. This means that there is almost a factor of 7 more cells compared to particles. On the other hand, cells are uniformly distributed in space and only $\approx$70 276 cover the cloud in the initial set-up of an almost perfectly spherical cloud. This should be compared to the $\approx 10^5$ particles constituting the cloud in the high-resolution SPH run. A comparison like this is still not straightforward due to the fact that SPH uses particles as non-independent resolution elements. This means that each particle is not a carrier of information without neighbours to smooth over, and the effective number of resolution elements is more or less set by the kernel shape and number of neighbours to smooth over.

Resolution affects the convergence of hydrodynamical simulations. A cut-off is always introduced on the scale of the spatial resolution below which instabilities cannot be resolved. This often serves as a source of numerical viscosity. For most of the codes used in the comparison, we have varied the resolution in order to obtain an understanding of how this changes the cloud morphology, mass loss and fragmentation time (see Table 1). Fig. 7 shows the outcome of, from top to bottom, ENZO˙64, ENZO_128, ENZO_256, GAS_1M and GAS_10M. In the grid simulations we conclude that, while the compression and elongation of the cloud are relatively similar, the detailed way the cloud fragments is resolution dependent as the ICs are (Jones, Ryu & Tregillis 1996). In ENZO_64, a mode of the KHI symmetric with respect to the symmetry axis of the cloud is dominant. This mode becomes less dominant as resolution is increased (ENZO_128) and has not yet developed by $t = 1.5\tau_{\rm KH}$ in ENZO_256. Going to higher resolution we see more and more small-scale instabilities developing which enhance mixing of the cloud material with the background flow. Numerical diffusion is stronger in low-resolution simulations which is why parts of the cloud survive longer in the higher resolution runs. The different SPH simulations are qualitatively very similar. Instabilities cannot be resolved in GAS_1M nor in GAS_10M. However, we note a weak large-scale RTI on the cloud front at $t = 2.25\tau_{\rm KH}$ in GAS_10M, which is absent in GAS_1M.

The general description above is again quantified by studying the cloud mass fraction at each time-step, see Fig. 8. In this plot we have also added an extra low-resolution SPH simulation using only 10^5 particles. The grid simulations show a clear trend of dissolving the cloud quickly after $\sim\tau_{\rm KH}$ regardless of resolution while the SPH simulations only show a steady mass loss due to the material ablated into the trailing vacuum. Decreasing the SPH resolution causes the mass fraction to rise above the initial value during the initial phase and mass is lost more rapidly for $t > \tau_{\rm KH}$. The latter effect is most probably due to the increased mass of each particle, causing each particle interaction to transfer momentum in a more violent, 'bullet-like' fashion.

5.2 SPH versus grid resolution criteria

In the study of Mac Low & Zahnle (1994), simulations of the impact of comet Shoemaker–Levy with Jupiter were carried out using the ZEUZ-2D grid code (Stone & Norman 1992a). They found that a minimum of 25 grid cells per cloud radius was required to follow the evolution correctly. This resolution is reached in all of the high-resolution grid simulation that we have performed, but it is very important to note that the destruction of the cloud is captured even in the lowest resolution runs, where we only have seven cells per radius. In the case of SPH it is, as mentioned in Section 5.1, more difficult to apply this criterion. The most conservative translation of the criterion is to use 25 non-overlapping smoothing kernels per radius. This is indeed a lower limit to the resolution as the cubic spline smoothing kernel used in our SPH tests cannot exactly be interpreted as a grid cell. The kernel is given a radius allowing it to encompass 32 particles, and the strength of the kernel falls off rapidly. At half the kernel radius (at h), only 1/4 of the kernel's central value remains (Monaghan 1992), indicating that we probably have more resolution elements than in the non-overlapping kernel case. To safely test the resolution criterion, we anyway adopt the conservative 25 independent kernel interpretation in this section.

In order to investigate this we perform two additional simulations using ENZO and GASOLINE. Any uniform spherical distribution of $N_{\rm p}$ particles using a kernel smoothing over the n nearest neighbours has $n_{\rm k} = (1/2)(N_{\rm p}/n)^{1/3}$ independent smoothing kernels covering one radius. By having $n_{\rm k} = 25$ and $n = 32$ we see that we require $N_{\rm p} = 4 \times 10^6$ in the cloud only. This is to be compared with the requirement using grid codes which is $\approx$65 450 cells, a substantial difference in computation and storage. We use a smaller box in order to manage the large simulation required for SPH. In units of the cloud radius $R_{\rm cl}$, the sides are $\{L_x, L_y, L_z\} = \{4, 4, 12\}$ where we centre the cloud at $\{x, y, z\} = \{2, 2, 3\}$. The smaller box will give us a set-up that is not 'as clean' as the previous ones as the backflow and lateral bow shock interacts with the cloud in the later evolution due to the periodic boundary condition that are necessary to impose (inflowing boundary conditions are not possible in the current version of GASOLINE). We will however fully trace the evolution past the important $\tau_{\rm KH}$, which is estimated in the same way as in Section 3. To facilitate computations we used a density contrast $\chi = 20$ for this test. This reduces the total number of SPH particles to $\approx 1.36 \times 10^7$. To optimize the conditions for the SPH simulations we have adopted a lower viscosity setting than normally used; $\alpha = 0.1$ and $\beta = 1.5$. This is done in order not to suppress possible growth of instabilities while still capturing shocks (see Section 6.1 for a discussion). The grid simulation is performed as before but now using a static grid of size $100 \times 100 \times 300$. In order to see the direct effect of the high-resolution run we have also performed a simulation using the same number density of particles in the cloud as in GAS_10M but with the new density contrast, viscosity setting and box size. The visual outcome of the simulations can be seen in Fig. 9. The conclusion of the previous sections remains valid; the initial phase of the evolution is very similar for the grid and SPH simulations. However, later evolution of the cloud in the grid simulations shows surface instabilities developing leading to fragmentation and mixing of material after $t = \tau_{\rm KH}$. The cloud in

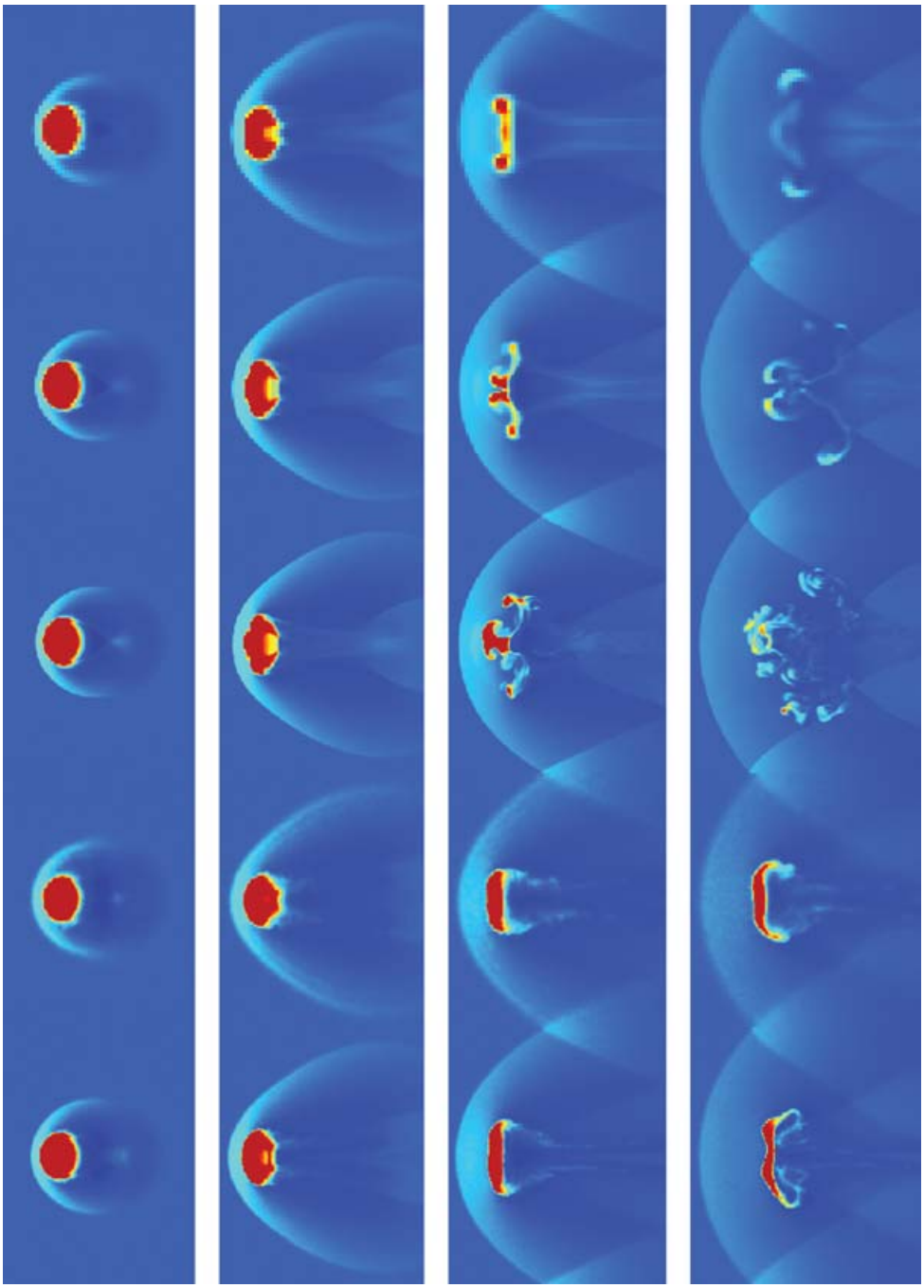

Figure 7. Resolution study for ENZO and GASOLINE. The panels show density slices of, from top to bottom, ENZO_64, ENZO_128, ENZO_256, GAS_1M and GAS_10M for $t = 0.25$, 0.75, 1.5 and $2.25\tau_{\rm KH}$. We see that resolution changes the phase of the instabilities in the grid simulations while the destruction time is the same. Higher resolution also shows less diffusion and better resolves small-scale fragments. The GASOLINE runs are not able to resolve small-scale instabilities at all.

the SPH simulation does not fragment and suffers only from lateral elongation and ablation.

The differences are small between the high resolution and standard SPH simulation with only minor morphological differences probably owing to different capturing of the more complicated shock structure in this new set-up. A test of the standard resolution simulation using larger viscosity setting was also performed (not shown here) which produces identical results, assuring us that the specific viscosity setting is not unphysically low.

We conclude that the observed differences between grid and SPH methods are not related to resolution and that convergence must be reached by other means.

5.3 Initial seeds

As partly shown in the previous test, the development of the instabilities, particularly during the non-linear stages, is sensitive to the exact definition of the ICs. This is because they set the seed

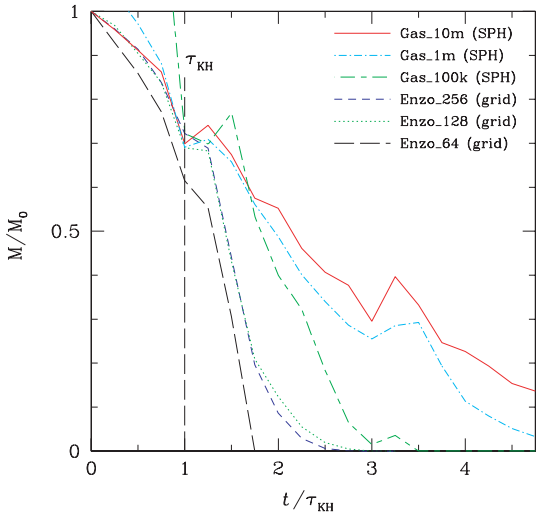

Figure 8. The evolution of the cloud mass fraction for different resolutions. As the resolution of the grid simulations is increased from 64 to 128 to 256 cells across the wind tunnel, the amount of mass increases a little but converges. Increasing the resolution of the SPH simulations does not decrease the amount of mass lost, rather the opposite, perhaps due to the momentum transfer due to massive particles acting like 'bullets'.

perturbations out of which the instabilities grow. However, while the mixing of the cloud material with the background medium is affected by small-scale motions that arise from the small unstable scales, the cloud disruption is mostly the result of the development of the large-scale perturbations. As an example of this in Fig. 10 we show the evolution of the cloud–wind interaction but with ICs set directly from the analytic definition. Thus in this case the ICs are free of noise and are purely symmetric. A base grid of (32 × 32 × 128) was used with two additional levels of refinement with refinement ratio of 4 placed dynamically in regions where the relative change in density, $\Delta\rho/\rho$ exceeded 20 per cent. This corresponds to an effective resolution of 512 × 512 × 2048 in the finest grids, which reduces the level of perturbation with respect to the previous cases.

As shown in panel B of Fig. 10 the most destructive mode has a different phase than in the cases illustrated above for the corresponding grid-based codes. However, as in the previous cases, by $t = 2.5\tau_{KH}$ (panel D) the cloud has been completely reduced to debris by the instabilities. This shows that despite differences in the appearance of the cloud gas distribution its fundamental fate of disruption and subsequent mixing on a time-scale of a few τ_{KH} is independent of the specific definition of the ICs.

6 WHY SO DIFFERENT?

What is the reason for the observed discrepancies between simulations carried out using SPH and grid-based techniques? Differences between SPH and grid-based results have been discussed before in the literature (Frenk & et al 1999; Pearce et al. 1999; Thacker et al. 2000; Ritchie & Thomas 2001; Tittley, Pearce & Couchman 2001; Springel & Hernquist 2002; Marri & White 2003; O'Shea et al. 2005) in different contexts to this study. While AV is the most obvious focus for criticism of SPH it is not the main reason for the differences observed in this test. We will show this in Section 6.1 before focusing on the almost complete suppression of KHIs (and RTIs) in SPH simulations of this test and present an explanation of why this occurs.

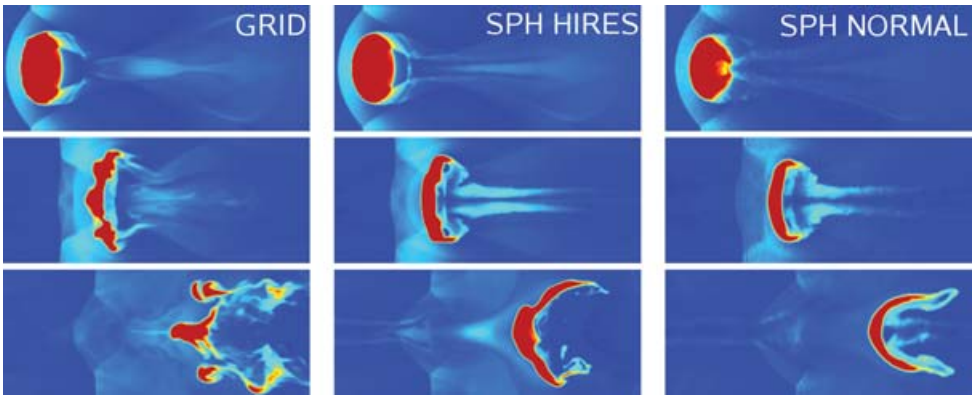

Figure 9. Each frame shows a density slice through the cloud centre at times $t = 0.5$, 1.0 and $1.5\tau_{KH}$ with densities varying from low (blue) to high (red). The grid (ENZO) simulation (left) shows instabilities developing on the surface causing the cloud to fragment, while these features are absent in the SPH (GASOLINE) simulation (middle and right).

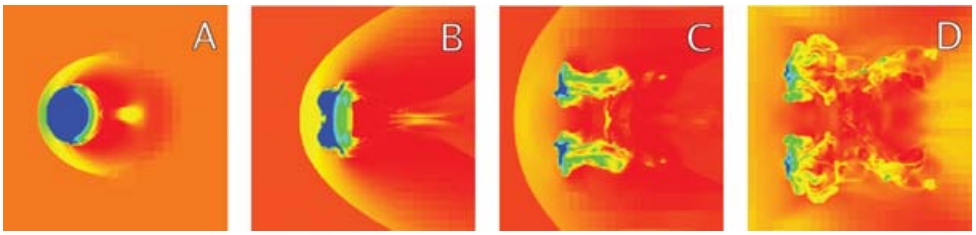

Figure 10. Evolution of the cloud with 'analytic' ICs using the CHARM code. Each frame shows a density slice through the cloud centre at times $t = 0.24$, 0.9, 1.7 and $2.5\tau_{KH}$ with densities varying from low (red) to high (blue).

6.1 Artificial viscosity

The AV β parameter in equation (15) is necessary for shock capturing and is required for SPH to work properly in unsmooth supersonic flows. In smooth flows where interparticle velocities are vanishing, no AV is required and is turned off (see equation 15). The α parameter has a less obvious meaning and the classical $\alpha = 1.0$ setting is most probably unphysical. It can be argued (e.g. Watkins et al. 1996) that α can roughly be interpreted as a Navier–Stokes shear plus bulk viscosity, even though the AV is only sensitive to flow properties such as interparticle travelling. Bulk viscosity is normally not important in fluid dynamics, except in the theory of attenuation of sound waves (e.g. Faber 1995). In numerical simulation its inclusion is for the most part to dampen the so-called post-shock ringing. Many grid-based techniques employ AV in order to stabilize the solutions from high-frequency oscillations occurring at sharp transitions in flux quantities. All of the grid methods in this paper, except for ENZO_ZEUS, use of Godunov's method. This means, among other things, that fluxes are calculated using Riemann solvers, hence not needing any inclusion of explicit AV terms except for very high Mach number shocks (Colella & Woodward 1984). Note however that there is always numerical viscosity due to resolution and truncation error in all simulation methods. In practice, this means that dynamics on the resolution scale is damped. To quantify the effect of this in the form of an effective viscosity term is not straightforward and requires well-defined problems with analytically known solutions to test against. The inclusion of AV leads us to one of the first possibilities for the observed discrepancy: we are not solving the same hydrodynamical equations in the different codes. By adding AV we are solving some kind of Navier–Stokes equation when we actually want to compare the solutions to the grid codes that, in this sense, are closer to the Euler equations.

Viscosity has two major effects on the processes we want to capture in this test.

(i) Dampening of small-scale velocity perturbations and random velocities.
(ii) Diffusion of post-shock vorticity and smearing of turbulence.

The effect of (i) will enter as a stabilizing factor for the growth of instabilities. Physical kinematic viscosity, ν, sets a cut-off for the size of the smallest eddies in turbulence (Shu 1992), below which turbulent motion is diffused. The effect of (ii) follows from the first one and is obvious from inspection of the vorticity transport equation (e.g. Shu 1992)

$$\frac{\partial \boldsymbol{\omega}}{\partial t} + \nabla \times (\boldsymbol{\omega} \times \boldsymbol{v}) = \nabla P \times \nabla \left(\frac{1}{\rho}\right) + \nu \nabla^2 \boldsymbol{\omega}, \tag{18}$$

where $\boldsymbol{\omega} \equiv \nabla \times \boldsymbol{v}$ is the vorticity. The two terms on the right-hand side can create or diffuse vorticity. The first term is the baroclinic term which is non-vanishing if we have non-aligned pressure and density gradients. This is the case in oblique shocks like in the bow shock of our cloud simulation. The second term is responsible for diffusing vorticity in space, i.e. taking local vorticity and spreading it into the general flow. This means that as soon as we have viscosity, we will dampen vorticity. Especially important is the vorticity generated in the post-shock flow, which should act to destabilize the cloud together with the surface instabilities.

A study on how AV dampens small-scale vorticity was made by Dolag et al. (2005). By using a low viscosity formulation of SPH they find higher levels of turbulent gas motions in the ICM and noted that shocked clouds tend to be unstable at earlier times. However, by looking at their fig. 3 we note that the overall difference in the cloud evolution is small. As we will see in the tests carried out below, lowering the AV does not necessarily lead to improved results.

In order to understand the effect of AV in our cloud–wind test we have performed three simulations with modified setting of the viscosity coefficients. These are GAS_10MAV1, GAS_10MAV2 and GAS_10AV3, see Table 1 for viscosity values. A simulation using the Balsara switch but with the standard ($\alpha = 1.0$, $\beta = 2.0$) was also performed. Fig. 11 shows the outcome of the simulations at $t = 0.25$, 0.75, 1.5 and $2.25\tau_{\rm KH}$. We can directly see the impact these terms have on the stability of the simulation. The standard $\alpha = 1.0$, $\beta = 2.0$ is the most stable one, most probably due to the unphysical use of the α bulk viscosity. The use of $\alpha = 0$ and $\beta = 2.0$ or the Balsara switch renders very similar visual results. This is because the Balsara switch turns of viscosity where $|\nabla \cdot \boldsymbol{v}|/(|\nabla \cdot \boldsymbol{v}| + |\nabla \times \boldsymbol{v}|)$ is significant, which is the case for shearing flows like on the surface of the cloud. Note that this is a very noisy quantity when measured using only 32 neighbours. By further lowering the shock capturing β viscosity we make the cloud even more unstable but it is not clear how physical this solution is. The shock front gets more blurred and we see strong post-shock ringing effects. The reason for the increased instability in the $\alpha = 0$, $\beta = 0.5$ and $\alpha = 0$, $\beta = 0.1$ case is most probably due to high speed particles travelling through the poorly captured shock region and transferring momentum inside the cloud, perturbing it in an unphysical way.

We have performed simulations similar in spirit to the SPH ones using ENZO-ZEUS. There is formally no need for linear viscosity using this method except for hypersonic flows, but it is interesting to study the effect of lowering $Q_{\rm AV}$ in the same way as β. Fig. 12 shows density slices from these simulations at $t = 1.5$ and $2.25\tau_{\rm KH}$. We see no impact on the cloud fragmentation except for minor morphological differences expected in turbulent regimes: $Q_{\rm AV}$ only serves to broaden the shock. Viscosity in grid-based techniques are not as fundamental as in SPH techniques, where it must be set large enough to properly reproduce the behaviour of a fluid and not a collection of particles.

We chose not to experiment with linear viscosity in ENZO-ZEUS as it is truly a viscous term with the same functional form as what is associated with the SPH α viscosity but is also sensitive to expansion. A comparison can therefore not be made on equal terms.

To conclude, we see from these simulations how lowering the AV outside shock regions will make the cloud in the SPH simulations less stable while losing the fluid behaviour for very low values. We still cannot obtain agreement with the grid-based codes which leads us to suspect that there are more fundamental reasons behind the discrepancies.

6.2 Resolving instabilities

In order to create an even simpler test problem to compare instabilities between codes, we carried out a classical KH test using GASOLINE and ENZO. We looked at the shearing motion of two gases of different densities and with small perturbations imprinted at the boundary. This captures the hydrodynamics at the surface of the cloud in the blob test.

The set-up is a periodic box with dimensions $\{L_x, L_y, L_z\} = \{1, 1, 1/32\}$, divided into two regions: one cold, high density and one warm, low density. The density and temperature ratio is $\chi = \rho_{\rm b}/\rho_{\rm t} = T_{\rm t}/T_{\rm b} = c_{\rm t}^2/c_{\rm b}^2$, putting the whole system in pressure equilibrium. The two layers are given constant and opposing shearing velocities, with the top layer moving leftward at a Mach number $\mathcal{M}_{\rm t} = v_{\rm t}/c_{\rm t} \approx 0.11$ and the bottom layer moving rightward at a Mach number $\mathcal{M}_{\rm b} = v_{\rm b}/c_{\rm b} \approx 0.34$ in the case of $\chi = 10$. The shear

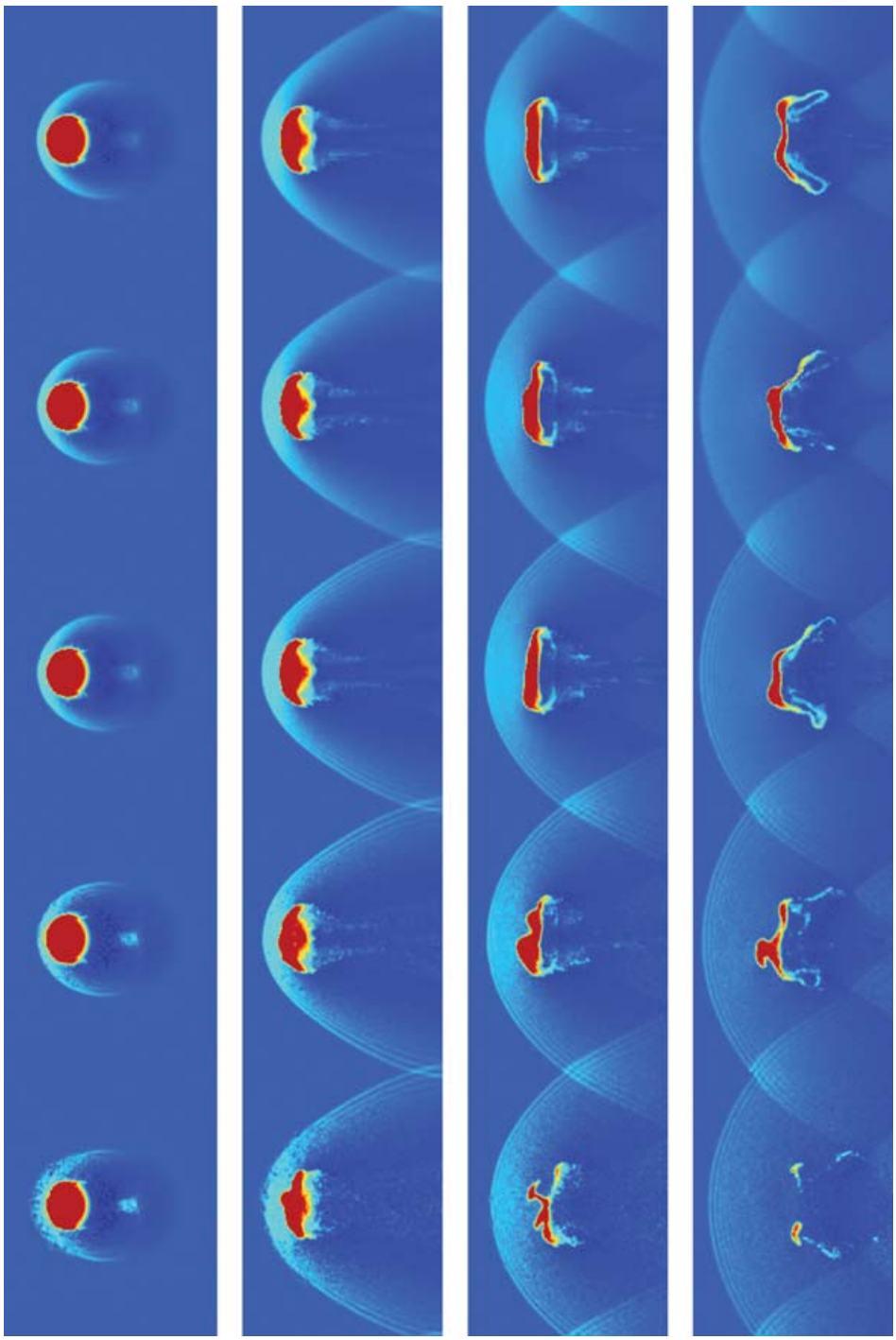

Figure 11. Viscosity study for GASOLINE. The panels show density slices of, from top to bottom, GAS_10M, GAS_BALS, GAS_10MAV1, GAS_10MAV2 and GAS_10MAV3 for $t = 0.25, 0.75, 1.5$ and $2.25\tau_{\rm KH}$. We can see how reducing shear viscosity and removing the bulk viscosity renders very similar results; the cloud destabilizes to a higher degree. By reducing the shock capturing viscosity the cloud destabilizes even further, most probably to an unphysical solution in the lower setting. The artificial post-shock ringing also gets more pronounced, as expected for lower viscosity settings.

velocity becomes $v_{\rm shear} = 0.68\, c_{\rm b}$ and the subsonic regime will assure growth of instabilities (Vietri et al. 1997). This set-up should mimic the growth of instabilities on the cloud surface.

To trigger instabilities we have imposed sinusoidal perturbation on the vertical velocity of the form

$$v_y(x) = \delta v_{\rm y} \sin(\lambda 2\pi x), \tag{19}$$

where $\delta v_{\rm y}$ is the amplitude of the perturbation in terms of the sound speed $c_{\rm b}$ and λ is the wavelength of the mode which we have put to 1/6 in all of out tests. The perturbation is limited to a central strip around the interface of thickness 5 per cent of the box size.

The ICs are again generated using particles for SPH. These are then mapped to a grid as explained in Section 4.1 to be used in the grid code, allowing a similar starting point for both codes. An

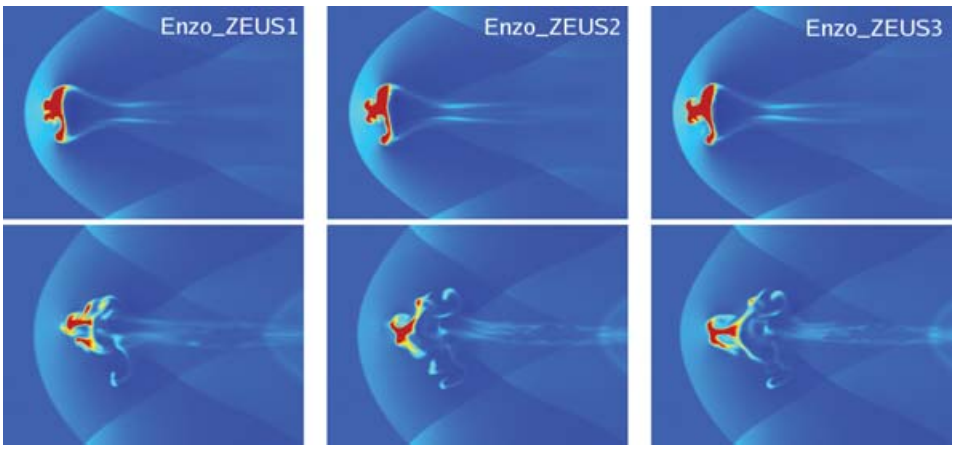

Figure 12. Viscosity study for ENZO-ZEUS. The panels show density slices of, left to right, ENZO_ZEUS1, ENZO_ZEUS2 and ENZO_ZEUS3 at $t = 1.5$ and $2.25\tau_{\rm KH}$. The outcome of the simulations shows little difference; only minor morphological changes are found. AV in ENZO-ZEUS only affects regions of strong compression and is therefore not crucially acting to damp hydrodynamical instabilities associated with the cloud.

important issue for this type of test is how the initial particles are distributed since this will introduce a certain amount of noise via discreteness. The most common techniques for this are the following.

(i) *Lattice.* Particles are ordered in a perfect grid. For a shearing layer test, this type of IC is optimal for grid codes as it traces the computational grid perfectly and suppresses all local density fluctuations.

(ii) *Poisson.* Particles are randomly distributed to generate the IC of our problem. This type of set-up generates local density variations, causing spurious pressure forces.

(iii) *Glass.* A Poisson particle distribution, with our IC set-up, is heated and relaxed until random velocities arising from pressure fluctuations are much smaller ($\lesssim$ few per cent) than the later imposed shear velocity (see Section 4.1).

Any IC with local density variations will trigger small-scale KHIs. We carried out this test using all three methods in order to illustrate their impact. The lattice is obviously perfect for grid codes, making a perfectly homogeneous gas. This quality does not automatically produce clean SPH ICs due to the averaging over nearby particles. The Poisson ICs are very noisy in both the grid and SPH case, even though grid codes tend to smooth the noise over the cell sizes. The glass IC is intuitively the closest IC for both methods producing a self-consistent and homogeneous initial state for SPH simulations while leaving only small fluctuations for both grid and SPH methods.

This set of simulations and their characteristics are summarized in Table 2, and Fig. 13 shows the results, from top to bottom, GRID1, GRID3 and SPH3. We choose to show only one of the SPH results since all of these runs give the same result. GRID1 and GRID3 illustrate the difference between a highly idealized smooth set-up (GRID1) and one with small-scale noise (GRID3).

Table 2. Performed KH runs.

Resolution	χ	$\delta v/v_{\rm shear}$	IC	Name
ENZO				
{256, 256, 8}	8.0	1/80	Lattice	GRID1
{256, 256, 8}	10.0	1/40	Poisson	GRID2
{256, 256, 8}	10.0	1/40	Glass	GRID3
GASOLINE				
900 k part	8.0	1/80	Lattice	SPH1
1.1 M part	10.0	1/40	Poisson	SPH2
1.1 M part	10.0	1/40	Glass	SPH3

GRID1 nicely produces the KHIs and the growth time is in excellent agreement with that expected from equation (8). This growth is not as clean in GRID3, which is to be expected due to local noise in density which alters the visual outcome. However, the KHI is still well resolved and the growth time is comparable to the analytical expectation.

The outcome of the SPH simulation is again very different from the grids. Perturbations are damped out very quickly both in velocity and density regardless of choice of ICs, resolution, perturbation strength and viscosity. We conclude that SPH in the form used in astrophysical simulations to-date is unable to capture dynamical instabilities such as KH when density gradients are present. As we will show in the next section, the reason for this stems from the way hydrodynamical forces are calculated in SPH in regions with strong gradients.

6.3 Mind the gap

Fig. 14 shows a close-up of the SPH particles at the interface of the two fluids in SPH3 at $t = \tau_{\rm KH}$. There is a gap between them that has the size of an SPH smoothing kernel radius ($\sim 2h_{ij}$). This gap repeats periodically in each fluid, being smaller in the higher density fluid since the smoothing length (mean distance to the nearest 32 particles) is smaller there. This feature is found in all of our SPH KH simulations. It occurs very quickly and becomes more prominent with time. This phenomenon has been discussed before in the literature (e.g. Ritchie & Thomas 2001; Tittley et al. 2001; Okamoto et al. 2003), especially in the context of numerical overcooling (Pearce et al. 1999; Thacker et al. 2000; Springel & Hernquist 2002; Marri & White 2003) but no relation to resolving instabilities has been mentioned.

The gap can also be clearly seen in the cloud test simulation (Fig. 5). Even though the gas is streaming with high velocity on to the leading surface of the cloud, spurious pressure forces prevent it from making any physical contact. The reason that the cloud loses mass in the SPH simulation is due to the vacuum behind the cloud into which the cloud expands from its edges. Here the gradients become smooth and the gas can be removed by the pressure difference between the cloud and the ambient medium that streams past.

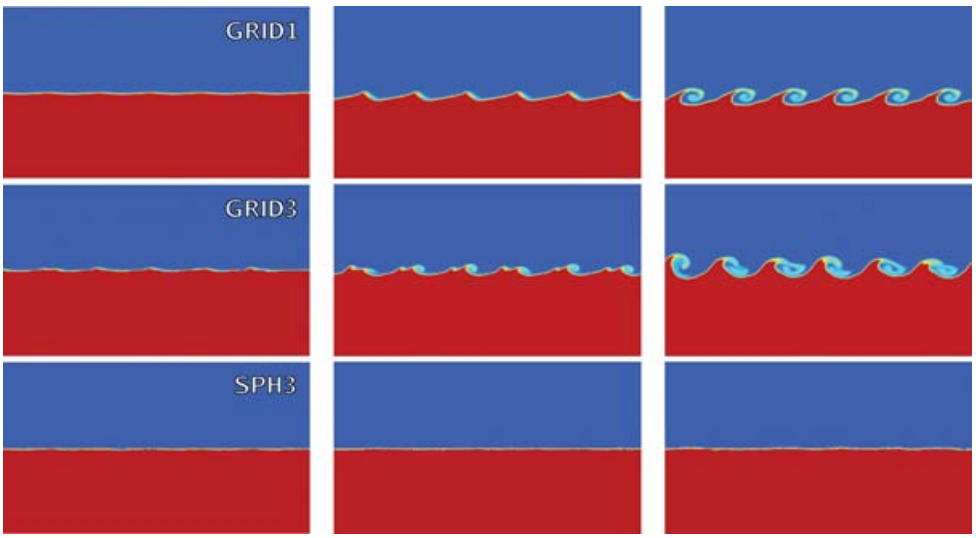

Figure 13. Density slices of, from top to bottom, GRID1, GRID3 and SPH3. The panels show the KH simulation at $t = \tau_{\rm KH}/3$, $2\tau_{\rm KH}/3$ and $\tau_{\rm KH}$. The grid simulations show clear growth of the KHI while this is completely absent in SPH.

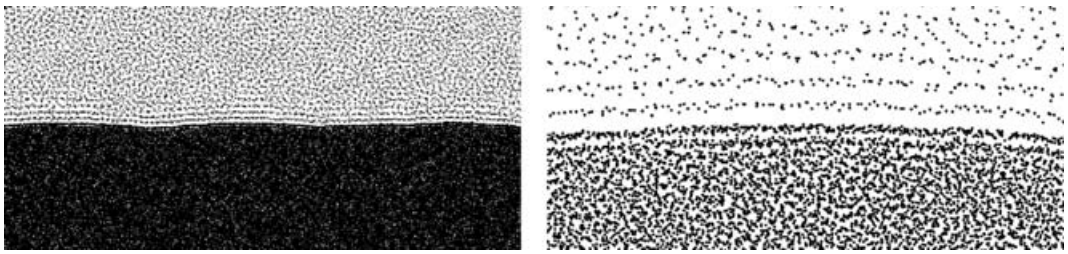

Figure 14. A close up view of the SPH particles at the boundaries between the shearing layers (left) and closer zoom in (right) for SPH3 at $\tau_{\rm KH}$. We can clearly see empty layers formed through erroneous pressure forces due to improper density calculations at density gradients. Even though the two fluids are moving relative to each other, the gap is so large that proper fluid interaction is severely decreased or even absent.

The effect can be explained in the following way: equation (14) is the force on each SPH particle coming from the summation over the 32 nearest neighbours. The pressure is given by $P \sim \rho T$ in the assumed case of an ideal gas. This force calculation formally assumes that temperature, and more importantly, density gradients are small within the smoothing kernel, where temperature is a quantity accumulated over time while density usually is re-estimated at each time-step. When a particle from a hot low-density region approaches a cold high-density region it will suddenly find a lot of neighbours at the edge of the smoothing sphere within the dense medium and its density will be overestimated. This leads to, through momentum conservation, a repulsive, fictitious, force on the particle, causing it to bounce back into the low-density region. This behaviour leads to the formation of a gap between the two phases of the size $\sim 2h_{ij}$, where h_{ij} is the effective smoothing kernel length, either obtained by using smoothing length or smoothing kernel averaging (Hernquist & Katz 1989), depending on the SPH implementation. Hot particles close to this gap will now have a strongly asymmetric distribution of particles around them resulting in an average pressure force pointing back into the vacuum layer. Particles then travel back into the empty region and the whole process is repeated. This particle migration and its associated pressure forces will act as an effective restoring force for the surface, a kind of tension. This together with the gap essentially removes multiphase behaviour from SPH. From the above arguments it is straightforward to see that in all standard formulations of SPH, any relaxed multiphase particle distribution must have an associated gap.

As mentioned above, this erroneous treatment of density contrasts has also been found to produce overcooling in galaxy formation simulations. Tittley et al. (2001) showed that in subsonic regimes this behaviour leads to fictitious accretion of particles on the lateral sides of gas clouds such as the simulations showed in this paper. Solutions to this problem has been attempted by several authors (e.g. Ritchie & Thomas 2001; Marri & White 2003) by reformulating SPH to more accurately treat the particle interactions at steep boundaries. While this seems to remove the gap to some extent, it is unclear how this will affect the simulations discussed here. Possible solutions to the problem such as improving the method of calculating gradients and minimizing their errors in SPH will be presented in a follow up paper by Read et al. (in preparation).

That erroneous density gradients are the root of the instability suppression becomes even more apparent by studying the KHI using a density contrast $\chi = 1$, in which the gap cannot form. We performed a simulation using GASOLINE in the same way as SPH3 described in Section 6.2 but now using 10^6 particles $\chi = 1$. With this vanishing density gradient, SPH is able to capture the KHI, see Fig. 15. The left-hand panel shows the KHI at $t = \tau_{\rm KH}$ for the standard $\alpha = 1.0$, $\beta = 2.0$ setting and the right-hand panel shows the same time-step but using $\alpha = 0.01$ and $\beta = 1.0$. The less evolved standard viscosity simulation points out the effects of viscosity

Figure 15. A zoom in of the SPH particles at the boundaries between the shearing layers for the isodensity SPH run with standard viscosity (left) and low viscosity (right) at $\tau_{\rm KH}$. The black and white regions are particles that belonged to the initially separated shearing layers. We clearly see growth of the KHI in the standard implementation of SPH, and even stronger for the low viscosity version. The simulation was performed with GASOLINE using 10^6 particles in the same way as SPH3 described in Section 6.2.

discussed in Section 6.1. Similar results have been recently found by Junk et al. (in preparation).

7 SUMMARY

In this paper we have carried out hydrodynamical simulations of a cold gas cloud interacting with an ambient hot moving gas using state of the art simulations codes. Striking differences were found between the two main techniques for simulating fluids. While grid codes are able to resolve and treat dynamical instabilities and mixing, these processes are poorly or not at all resolved by the current SPH techniques. We show that the reason for this is that SPH, at least in the standard usage and formulation, inaccurately handles situations where density gradients are present. In these situations, SPH particles of low density close to high-density regions suffer erroneous pressure forces due to the asymmetric density within the smoothing kernel. This causes a gap between regions of high-density contrast, essentially decoupling the different phases of the fluid.

This behaviour has implications for many astrophysical situations. The stripping of gas from galaxies moving through a gaseous medium has already been discussed in the literature. The origin of disc galaxies is an important unsolved problem. Perhaps the inability to disrupt accreting gas clouds is one reason why numerical calculations have failed to produce pure disc systems. Simulating star formation regions and feedback processes also relies on the correct ability to model turbulence and interacting multiphase fluids.

It should be noted that the behaviour of the grid and SPH methods agrees on time-scales shorter than those of typical dynamical instabilities such as the KHIs and RTIs. In our specific test of a cold cloud engulfed in a hot wind, there is good agreement in the early gas stripping phase occurring due to pressure differences arising in the Bernoulli zones. As soon as the large-scale instabilities have grown, the results of the different methods diverge. There are several possible solutions to this behaviour in SPH calculations which we will explore in a separate work.

ACKNOWLEDGMENTS

We acknowledge support from the European Science Foundation who funded an exploratory workshop in Wengen 2004 at which these tests were first discussed. FM and LM acknowledge support by the Swiss Institute of Technology through a Zwicky Prize Fellowship. OA would like to thanks Alessandro Romeo, Peter Englmaier and Mordecai-Mark Mac Low for valuable discussions. AG acknowledges the support from the Polish Ministry of Science through the grant 1P03D02626 and from the European Community's Human Potential Programme through the contract HPRN-CT-2002-00308, PLANETS. The AMR software (FLASH) used in this work was in part developed by the DOE-supported ASC/Alliance Centre for Astrophysical Thermonuclear Flashes at the University of Chicago. The FLASH calculations were performed at the Interdisciplinary Centre for Mathematical and Computational Modelling in Warsaw, Poland.

The ENZO, GASOLINE and GADGET-2 simulations, as well all of the analysis presented in this paper, were performed on the zBox1 and zBox2 supercomputers (http://krone.physik.unizh.ch/~dpotter/zbox/) at the University of Zürich.

REFERENCES

Abadi M. G., Moore B., Bower R. G., 1999, MNRAS, 308, 947
Anninos W. Y., Norman M. J., 1994, ApJ, 429, 434
Balsara D. S., 1995, J. Comput. Phys., 121, 357
Bryan G. L., Norman M. L., 1997, in Clarke D. A., West M. J., eds, ASP Conf. Ser. Vol. 123, Computational Astrophysics. Astron. Soc. Pac., San Francisco, p. 363
Bryan G. L., Norman M. L., Stone J. M., Cen R., Ostriker J. P., 1995, Comput. Phys. Commun., 89, 149
Chandrasekhar S., 1961, Hydrodynamic and Hydromagnetic Stability, International Series of Monographs on Physics. Clarendon, Oxford
Colella P., Glaz H. M., 1985, J. Comput. Phys., 59, 264
Colella P., Woodward P. R., 1984, J. Comput. Phys., 54, 174
Dolag K., Vazza F., Brunetti G., Tormen G., 2005, MNRAS, 364, 753
Doroshkevich A. G., Zeldovich I. B., 1981, Zh. Eksp. Teor. Fiz., 80, 801
Faber T. E., 1995, Fluid Dynamics for Physicists. Cambridge Univ. Press, Cambridge
Frenk C. S. et al., 1999, ApJ, 525, 554
Fryxell B. et al., 2000, ApJS, 131, 273
Gregori G., Miniati F., Ryu D., Jones T. W., 2000, ApJ, 543, 775
Hernquist L., Katz N., 1989, ApJS, 70, 419
Inogamov N. A., 1999, Astrophys. Space Phys. Rev., 10, 1
Jones T. W., Ryu D., Tregillis I. L., 1996, ApJ, 473, 365
Khokhlov A. M., 1998, J. Comput. Phys., 143, 519
Klein R. I., McKee C. F., Colella P., 1994, ApJ, 420, 213
Kravtsov A. V., 1999, PhD thesis, New Mexico State University
Kravtsov A. V., Klypin A., Hoffman Y., 2002, ApJ, 571, 563
Laney C., 1998, Computational Gasdynamics. Cambridge Univ. Press, Cambridge
Lattanzio J. C., Monaghan J. J., Pongracic H., Schwarz M. P., 1986, SIAM J. Sci. Stat. Comput., 7, 591
Leveque R. J., 1998, in Steiner O., Gautschy A., eds, Saas-Fee Advanced Course 27, Computational Methods for Astrophysical Fluid Flow. Springer, Berlin, p. 1
Mac Low M.-M., Zahnle K., 1994, ApJ, 434, L33
Mac Low M.-M., McKee C. F., Klein R. I., Stone J. M., Norman M. L., 1994, ApJ, 433, 757
Marri S., White S. D. M., 2003, MNRAS, 345, 561
Miniati F., Colella P. J., 2006, Comput. Phys. submitted (astro-ph/0608156)
Miniati F., Jones T. W., Ryu D., 1999, ApJ, 517, 242
Monaghan J. J., 1992, ARA&A, 30, 543
Mori M., Burkert A., 2000, ApJ, 538, 559
Murray S. D., White S. D. M., Blondin J. M., Lin D. N. C., 1993, ApJ, 407, 588
Nulsen P. E. J., 1982, MNRAS, 198, 1007

Okamoto T., Jenkins A., Eke V. R., Quilis V., Frenk C. S., 2003, MNRAS, 345, 429
O'Shea B. W., Nagamine K., Springel V., Hernquist L., Norman M. L., 2005, ApJS, 160, 1
Pearce F. R. et al., 1999, ApJ, 521, L99
Quilis V., Moore B., Bower R., 2000, Sci, 288, 1617
Regan J. A., Haehnelt M. G., Viel M., 2007, MNRAS, 374, 196
Ritchie B. W., Thomas P. A., 2001, MNRAS, 323, 743
Shu F. H., 1992, in Frank H. S., ed., Physics of Astrophysics, Vol. II. University Science Books, Mill Valley, CA, p. 476
Springel V., 2005, MNRAS, 364, 1105
Springel V., Hernquist L., 2002, MNRAS, 333, 649
Springel V., Yoshida N., White S. D. M., 2001, New Astron., 6, 79
Stadel J. G., 2001, PhD thesis, Univ. Washington
Stone J. M., Norman M. L., 1992a, ApJS, 80, 753
Stone J. M., Norman M. L., 1992b, ApJS, 80, 791
Thacker R. J., Tittley E. R., Pearce F. R., Couchman H. M. P., Thomas P. A., 2000, MNRAS, 319, 619
Tittley E. R., Pearce F. R., Couchman H. M. P., 2001, ApJ, 561, 69
van Leer B., 1977, J. Comput. Phys., 23, 276
van Leer B., 1979, J. Comput. Phys., 32, 101
Vietri M., Ferrara A., Miniati F., 1997, ApJ, 483, 262
Vikhlinin A., Markevitch M., Murray S. S., 2001, ApJ, 549, L47
Wadsley J. W., Stadel J., Quinn T., 2004, New Astron., 9, 137
Watkins S. J., Bhattal A. S., Francis N., Turner J. A., Whitworth A. P., 1996, A&AS, 119, 177

This paper has been typeset from a TEX/LATEX file prepared by the author.